Chapter 2
Electromechanical and Chemical Sensing at the Nanoscale: DFT and Transport Modeling

Amitesh Maiti

Abstract Of the many nanoelectronic applications proposed for near to medium-term commercial deployment, sensors based on carbon nanotubes (CNT) and metal-oxide nanowires are receiving significant attention from researchers. Such devices typically operate on the basis of the changes of electrical response characteristics of the active component (CNT or nanowire) when subjected to an externally applied mechanical stress or the adsorption of a chemical or bio-molecule. Practical development of such technologies can greatly benefit from quantum chemical modeling based on density functional theory (DFT), and from electronic transport modeling based on non-equilibrium Green's function (NEGF). DFT can compute useful quantities like possible bond-rearrangements, binding energy, charge transfer, and changes to the electronic structure, while NEGF can predict changes in electronic transport behavior and contact resistance. Effects of surrounding medium and intrinsic structural defects can also be taken into account. In this work we review some recent DFT and transport investigations on (1) CNT-based nano-electromechanical sensors (NEMS) and (2) gas-sensing properties of CNTs and metal-oxide nanowires. We also briefly discuss our current understanding of CNT–metal contacts which, depending upon the metal, the deposition technique, and the masking method can have a significant effect on device performance.

2.1 Carbon Nanotube Basics

A carbon nanotube (CNT) is geometrically equivalent to a single sheet of graphite sheet rolled into a seamless cylinder in which a graphene lattice point (n_1, n_2) coincides with the origin $(0, 0)$. Thus, if a_1 and a_2 are the two lattice vectors of

A. Maiti

Lawrence Livermore National Laboratory, Livermore, CA 94551, USA
e-mail: amaiti@llnl.gov

graphene, the CNT circumference is equal to the length of the vector $(n_1\boldsymbol{a}_1 + n_2\boldsymbol{a}_2)$, while the CNT chiral angle θ is defined as the angle between vectors $(n_1\boldsymbol{a}_1 + n_2\boldsymbol{a}_2)$ and $\boldsymbol{a}_1$. With the choice of lattice vectors as in Fig. 2.1a, the chiral angle and diameter of a CNT are given respectively by the following formulas:

$$\theta = \tan^{-1}\left[\sqrt{3}n_2/(2n_1 + n_2)\right] \tag{2.1}$$

and

$$d = a\sqrt{\left(n_1^2 + n_1 n_2 + n_2^2\right)}/\pi, \tag{2.2}$$

where $a = |a_1| = |a_2| \sim 2.45$ Å is the lattice constant of graphene. The CNT diameter and chirality, and therefore its atomic geometry, are completely specified by the two integers (n_1, n_2), which are referred to as the chiral indices of the CNT. Because of the symmetry of the graphene lattice, a nanotube of any arbitrary chirality can be defined in the range $n_1 \geq n_2 \geq 0$ and $n_1 > 0$, which implies that the chiral angle θ for all CNTs lies between 0 and 30°. CNTs with the extreme chiral angles of 0 and 30° have special names: a CNT with $\theta = 0$ (i.e., $n_2 = 0$) is called *zigzag*, while a CNT with $\theta = 30°$ ($n_1 = n_2$) is called *armchair*. The names armchair and zigzag simply reflect the shape of the open edges of these CNTs (Fig. 2.1b, c). CNTs with any other chiral angles (i.e., $0 < \theta < 30°$) are called *chiral*.

As a CNT is just a rolled-up graphene sheet, one can obtain a good approximation to the CNT electronic structure simply by applying an appropriate boundary condition to the electronic structure of a graphene sheet, with a small perturbation due to the finite cylindrical *curvature* of the CNT surface. The boundary condition for a CNT with chiral indices (n_1, n_2) corresponds to the coincidence of the (n_1, n_2) lattice point of graphene with the origin $(0, 0)$. Taking into account small effects due to curvature, such boundary conditions lead to the following important result [1–6]: all *armchair* tubes are metallic; CNTs with $n_1 - n_2 = 3n$ (n = any positive integer), which include the $(3n, 0)$ *zigzag* tubes as a special class, are quasimetallic (small bandgap $\sim$10 meV or less, arising from curvature effects); and CNTs with $n_1 - n_2 \neq 3n$ are semiconducting, with a bandgap decreasing as $1/d$ as a function of tube diameter d (thereby converging to the zero bandgap of graphite in the limit $d \rightarrow \infty$). The presence of contact resistance and thermal effects often makes it difficult to experimentally distinguish between metallic and quasimetallic tubes. Thus for simplicity, experimentalists often classify CNTs as either metallic or semiconducting, and we follow the same convention in the discussion below. In spite of significant efforts, researchers have so far been unable to control the chiral indices of the synthesized CNTs (except, perhaps some control on the diameter). Therefore, given the preceding condition for metallic and semiconducting tubes, one could expect a random mix with roughly one-third metallic and two-third semiconducting CNTs. In our discussion so far it has been implied that the CNTs consist of only a single graphitic layer. Interestingly, such tubes, commonly called

(a) Graphite Sheet   (b) Armchair CNT   (c) Zigzag CNT
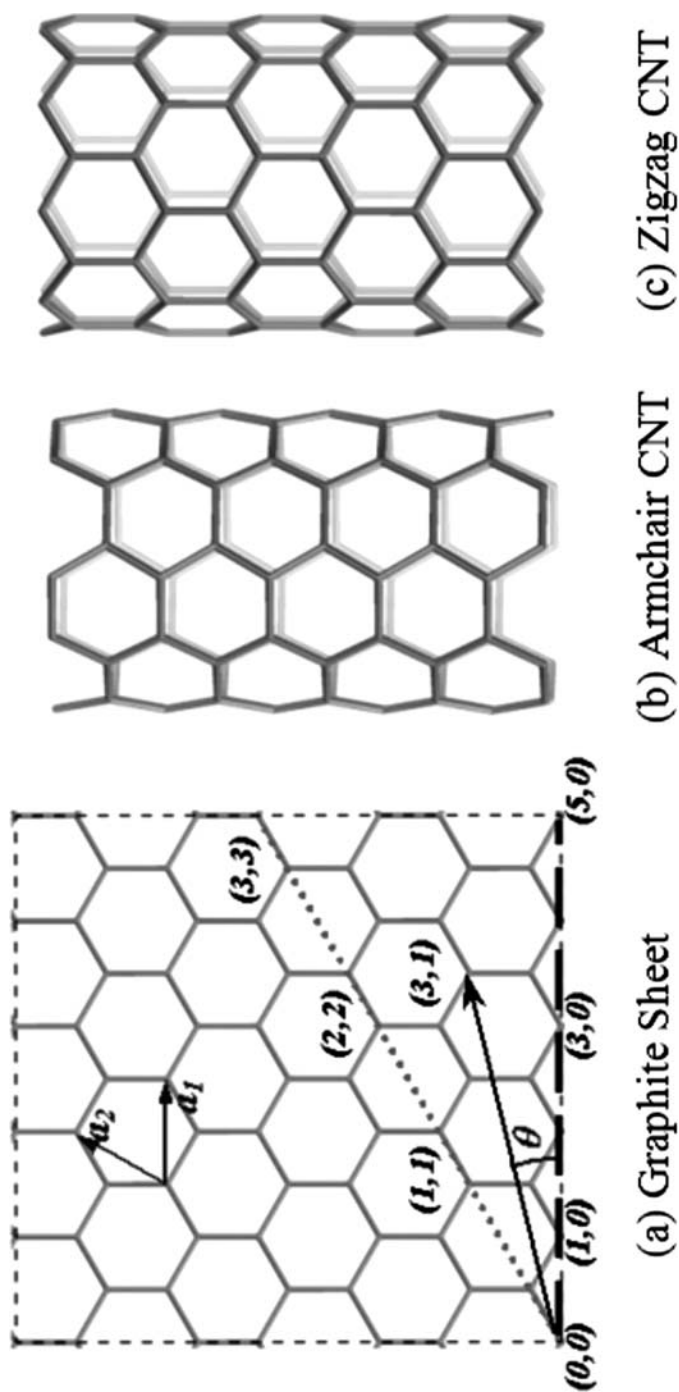
Fig. 2.1 Carbon nanotube (CNT) basics. (a) A graphene sheet with lattice vectors a_1, a_2. A few lattice points are indicated, as is the chiral angle θ for a (3, 1) CNT. *Dotted* and *dashed lines* are drawn along circumferences of *armchair* and *zigzag* tubes, respectively; (b) a (5, 5) *armchair* tube; (c) a (9, 0) *zigzag* tube

single-walled nanotubes (SWNTs), were discovered 2 years after the initial discovery of CNTs that consisted of several concentric layers. Such objects, now called multiwalled nanotubes (MWNTs), usually exhibit metallic characteristics.

More than 15 years after its initial discovery, CNTs continue to be one of the hottest research areas in all of science and engineering. The interest is driven by the possibility of several commercial applications [7–11], including field emission-based flat panel displays, transistors, quantum dots, hydrogen storage devices, structural reinforcement agents, chemical and electromechanical sensors, nanoscale manipulators, probes, and tweezers. At the same time, the highly regular atomic structure of CNTs and the large degree of structural purity make them accessible to accurate computer modeling using a variety of theoretical techniques. In fact, ever since the discovery of the CNT it has provided a fertile ground for theoretical simulations and analysis. The prediction of the dependence of CNT's electronic structure on its chirality [1–3] came within a year of the initial experimental discovery [12]. Since then, there have been a significant number of theoretical investigations [13–18] of growth mechanisms, structure and energetics of topological defects, mechanical and electrical response to various kinds physical perturbation, field-emission from tips of metallic CNTs, electronic effects of doping and gas adsorption, chemical reactivity, interaction with polymers, capillary effects, CNT–metal contacts, H- and Li-storage, thermal conductivity, encapsulation of organic and inorganic material, optical properties, as well as intrinsic quantum effects like quantized conductance, Coulomb Blockade, Aharonov–Bohm effect, Kondo effect, and so on. Computational approaches used in the above work include solving diffusion equations, quantum-mechanical (QM) simulations (DFT, tight-binding, and semiempirical methods), classical molecular dynamics, kinetic Monte Carlo, Genetic algorithms, and Green's-function-based electronic transport theory.

Focusing on electronics applications of CNTs, the areas that have received the most attention have been displays, transistors, and sensors. Displays require metallic CNTs, and naturally involve MWNTs. Although single-SWNT-based transistors have been demonstrated for a few years now, there are a number of serious challenges to be overcome for CNT-based integrated chips to become practical. Much of the recent work has therefore focused on sensor applications. Two types of sensors that have received the most attention are the electromechanical sensors and gas/chemical/bio sensors. Both of these operate on the basis of changes in electrical conductance upon either an external mechanical stimulus or the adsorption of an analyte. The electrical conductance changes can be directly related to either changes in the electronic band structure due to mechanical perturbation, or partial electron transfer between the analyte and the nanotube. Such studies can be carried out efficiently by the present-day DFT codes (in addition to semiempirical methods, which have also been employed in situations where parameters exist). As transport through nanotubes is essentially ballistic, one could use electronic transport calculations based on nonequilibrium Green's function (NEGF) to compute intrinsic conductance of the device (assuming "ideal" contacts).

2.1.1 *SWNTs as Nanoelectromechanical Sensors*

In a pioneering experiment Tombler et al. [19] demonstrated that when the middle part of a segment of a metallic SWNT suspended over a trench is pushed with an atomic force microscope (AFM) tip, the electrical conductance of the tube dropped by more than two orders of magnitude beyond a deformation angle of $\sim 14°$. The effect was found to be completely reversible; i.e., through repeated cycles of AFM-deformation and tip removal, the electrical conductance displayed a cyclical variation with constant amplitude.

The drop in conductance in the AFM-deformed tube was much higher than the computationally predicted values for tubes bent under mechanical duress. Both tight-binding [20] and semiempirical extended-Hückel type calculations [21] concluded that even under large bending angles the reduction in electrical conductance was less than an order of magnitude. For AFM-deformed nanotubes, in contrast, O(N) tight-binding calculations [22] show that beyond a critical deformation several C-atoms close to the AFM tip become sp^3-coordinated. The sp^3 coordination ties up delocalized π-electrons into localized σ-states. This would naturally explain the large drop in electrical conductivity, as verified by explicit transport calculations.

Realizing that an AFM-deformed tube also undergoes tensile stretching, and a stretched tube belonging to certain chirality class can undergo significant changes in electrical conductance upon stretching, we carried out independent calculations to check the above sp^3 coordination idea. The smallest models of CNTs necessary in such simulations typically involve a few thousand atoms, which makes first-principles quantum mechanics simulations unfeasible. Therefore, as described below, we carried out a combination of first-principles DFT [23–25] and classical molecular mechanics [26, 27] to investigate structural changes in a CNT under AFM-deformation. Bond reconstruction, if any, is likely to occur only in the highly deformed, nonstraight part of the tube close to the AFM-tip. For such atoms, we used a DFT-based quantum mechanical description (~ 150 atoms including AFM-tip atoms), while the long and essentially straight part away from the middle was described accurately using the universal force field (UFF) [28]. For DFT calculations we employed the code DMol^3 [3, 29–32] distributed by Accelrys, Inc. The electronic wave functions were expanded in a double-numeric polarized (DNP) basis set with a real-space cutoff of 4.0 Å. Such a cutoff reduces computational requirements without significantly sacrificing accuracy, as has been explicitly verified in this and many other numerical experiments. An all-electron calculation was carried out on a "medium" integration grid using a gradient-corrected exchange-correlation functional due to Perdew, Burke, and Ernzerhof [33]. For calculations with periodic supercells (as described in Sects. 2.1.2, 2.1.3, and 2.2.1) we performed accurate Brillouin zone integration by a careful sampling of k-points [34]. Also, in order to estimate charge transfer to adatoms, the partial charge on each atom was computed using the Mulliken population analysis [35].

Because of known differences in electronic responses of zigzag and armchair tubes to mechanical deformation, we studied a (12, 0) zigzag and a (6, 6) armchair
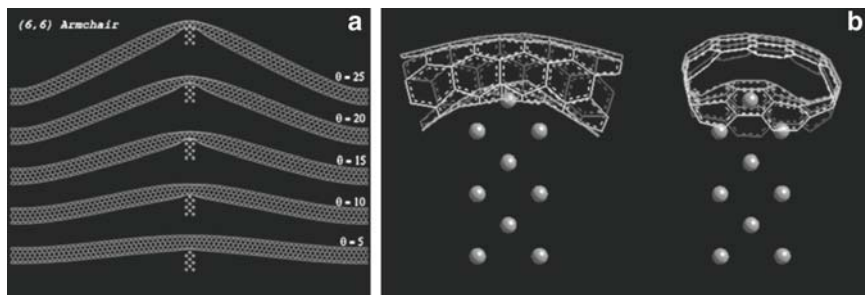
Fig. 2.2 (**a**) AFM deformation of a (6, 6) tube by a Li-needle. Respective deformation angles are indicated. (**b**) QM clusters at 25° of deformation showing no signs of sp^3 coordination

tube, each consisting of 2,400 atoms. The AFM tip was modeled by a 6-layer deep 15-atom Li-needle normal to the (100) direction, terminating in an atomically sharp tip (see Fig. 2.2) [36]. To simulate AFM-tip-deformation, the Li-needle was initially aimed at the center of a hexagon on the bottom-side of the middle part of the tube. The Li-needle tip was then displaced by an amount δ toward the tube along the needle-axis, resulting in a deformation angle $\theta = \tan^{-1}(2\delta/L)$, L being the nonstretched length of the tube. At each end of the tube, a contact region was defined by a unit cell plus one atomic ring (a total of 36 and 60 atoms for the armchair and the zigzag tube, respectively). The whole tube was then relaxed by UFF keeping the needle atoms and the end contact regions of the tube fixed. The contact region atoms were fixed in order to simulate an ideal nondeformed semi-infinite CNT lead, and to ensure that all possible contact modes were coupled to the deformed part of the tube. Following the UFF relaxation, a cluster of 132 C-atoms for the (6, 6) tube, and a cluster of 144 C-atoms for the (12, 0) tube were cut out from the middle of the tubes. These clusters (plus the AFM-tip atoms), referred to below as the QM clusters, were further relaxed with the DFT-code DMol^3 [3, 29] with the end atoms of the cluster plus the Li-tip atoms fixed at their respective classical positions.

Figure 2.2b displays the tip-deformed QM-cluster for the (6, 6) tubes at the highest deformation angle of 25° considered in these simulations. Even under such large deformations, there is no indication of sp^3 bonding [the same is true for a (12, 0) tube], and the structure is very similar to what was previously observed for a (5, 5) tube [36]. The absence of sp^3 coordination is inferred on the basis of an analysis of nearest-neighbor distances of the atoms with the highest displacements, i.e., the ones closest to the Li-tip. Although for each of these atoms the three nearest neighbor C-C bonds are stretched to a length between 1.45 and 1.75 Å, the distance of the fourth neighbor, required to induce sp^3 coordination is greater than 2.2 Å for all tubes in our simulations. The electronic charge density in the region between a C-atom and its fourth nearest neighbor is negligibly small, and none of the C-C-C angles between bonded atoms in the vicinity of the tip deviates by more than a few degrees from 120°, suggesting that the C-atoms near the AFM-tip essentially remain sp^2-coordinated. In order to test any possible dependence on the choice of

our tip, we also performed limited calculations with a close-capped (5, 5) CNT as the AFM tip, and the results were very similar to that obtained with a Li-tip.

2.1.1.1   Transport Calculations

Following structural relaxation of the CNTs as described above, we computed the transmission and conductance through the deformed CNT using NEGF formalism. A brief description of the method is provided below.

Electron transport through molecular wires like SWNTs is essentially ballistic, i.e., highly coherent with little scattering and very long mean free paths. Ohm's law completely breaks down in this regime. Such transport is best described by an energy-dependent transmission function $T(E)$, which strongly depends on the (discrete) electronic levels of the molecular wire (in our case, a nanotube), the levels in the (usually metallic) leads or electrodes, and broadening of the electronic levels in the wire because of chemical coupling to the electrodes [37–42]. Such physics is most conveniently described by the NEGF formalism. The starting point is the Green's function of an *isolated* system at an energy E, which is defined by the following equation:

$$(E \cdot S_{ij} - H_{ij})G^{R,jk} = \delta_i^k, \tag{2.3}$$

where δ_i^k is the Kronecker delta, and $S_{ij} = <i|j>$ and $H_{ij} = <i|H|j>$ are the overlap and Hamiltonian matrix elements between electronic states i and j, respectively. However, we are interested in systems in which a nanoscale region is coupled with two semi-infinite electrodes at the two ends (the so called *two-probe* system). In such a system, the coupling to the electrodes (mathematically expressed in terms of the so-called *self-energy* matrices Σ) modifies (2.1) to the form

$$(E \cdot S_{ij} - H_{ij} - \Sigma_{L,ij} - \Sigma_{R,ij})G^{R,jk} = \delta_i^k. \tag{2.4}$$

In the above equation $\Sigma_{L,R}$ are the retarded self-energies of the left and the right semi-infinite contacts. The transmission at energy E is then found from the following equation:

$$T(E) = G^{R,ij}\Gamma_{L,jk}G^{A,kl}\Gamma_{R,li}, \tag{2.5}$$

where $\Gamma_{L,R} = i\left(\Sigma_{L,R}^R - \Sigma_{L,R}^A\right)$ are the couplings to the left and right leads and the superscripts R and A represent retarded and advanced quantities, respectively. Finally, the total conductance of the tube is computed using the Landauer-Büttiker formula [43, 44]:

$$G = \frac{2e^2}{h} \int_{-\infty}^{\infty} T(E)\left(-\frac{\partial f_0}{\partial E}\right)dE, \tag{2.6}$$

$f_0(E)$ being the Fermi-Dirac function. The electronic states in the system, and more specifically the various matrix elements can be obtained either from first-principles or semi-empirical (e.g., tight-binding) quantum mechanical treatments. Also, if the interest is to investigate changes to the *intrinsic* electrical conductance of the nanotube, a common trick is to define "ideal" semi-infinite contacts on the basis of defect-free unstrained pieces of the pristine CNT. Such a procedure bypasses the necessity to model explicit metallic contacts, which is likely to involve additional chemical complexities on the top of extra computational burden.

The electrons in our model were described using a nearest-neighbor sp^3-tight-binding Hamiltonian in a nonorthogonal basis. The parameterization scheme explicitly accounts for effects of strain in the system through a bond-length-dependence of the Hamiltonian and the overlap matrices H_{ij} and S_{ij} [45].

Our results indicate that the conductance remains essentially constant for the (6, 6) armchair tube up to deformation as large as 25°. However, for the (12, 0) tube the conductance drops by a factor of ~0.3 at 15°, two orders of magnitude at 20°, and four orders of magnitude at $\theta = 25°$. As sp^3 coordination could be ruled out, the only logical explanation of the observed behavior could be due to stretching. We verified that by computing conductance changes due to pure tensile stretching and comparing the results with that of AFM-deformed tubes (Fig. 2.3). It should also be noted that the (12, 0) tube displays only a 70% drop in electrical conductance at $\theta = 15°$, while the experimental tube in Tombler et al. [19] underwent more than two orders of magnitude drop. This can be explained by the fact that the (12, 0) tube has a diameter of only ~1 nm, while the experimental tube was of diameter ~3 nm. A (36, 0) CNT, with diameter similar to the experimental tube, indeed displays a much higher drop in electrical conductance (Fig. 2.3).

In order to explain the differences in conductance drops of the armchair (6, 6) and the zigzag (12, 0) tubes as a function of strain, we turn to the literature where a considerable amount of theoretical work already exists [46–51]. An important result [50] is that the rate of change of bandgap as a function of strain depends on the CNT chiral angle θ, more precisely as proportional to $\cos(3\theta)$. Thus, stretched armchair tubes ($\theta = 30°$) do not open any bandgap, and always remain metallic. On the other hand, a metallic $(3n, 0)$ zigzag tube ($\theta = 0$) can open a bandgap of ~100 meV when stretched by only 1%. This bandgap increases linearly with strain, thus transforming the CNT into a semiconductor at a strain of only a few percent. In general, all metallic tubes with $n_1 - n_2 = 3n$ ($n > 0$) will undergo the above metal-to-semiconductor transition, the effect being the most pronounced in metallic zigzag tubes. An experiment as in Tombler et al. [19] is therefore expected to show a decrease in conductance upon AFM-deformation for all nanotubes except the armchair tubes. Researchers are also beginning to explore electrical response of squashed CNTs [52–54] where sp^3 coordination is a possibility.

In addition to the above results for metallic CNTs, theory also predicts that [50] for semiconducting tubes ($n_1 - n_2 \neq 3n$), the bandgap can either increase (for $n_1 - n_2 = 3n-2$) or decrease (for $n_1 - n_2 = 3n-1$) with strain. These results have prompted more detailed experiments on a set of metallic and semiconducting CNTs deformed with an AFM-tip [55], as well as on CNTs under experimental tensile
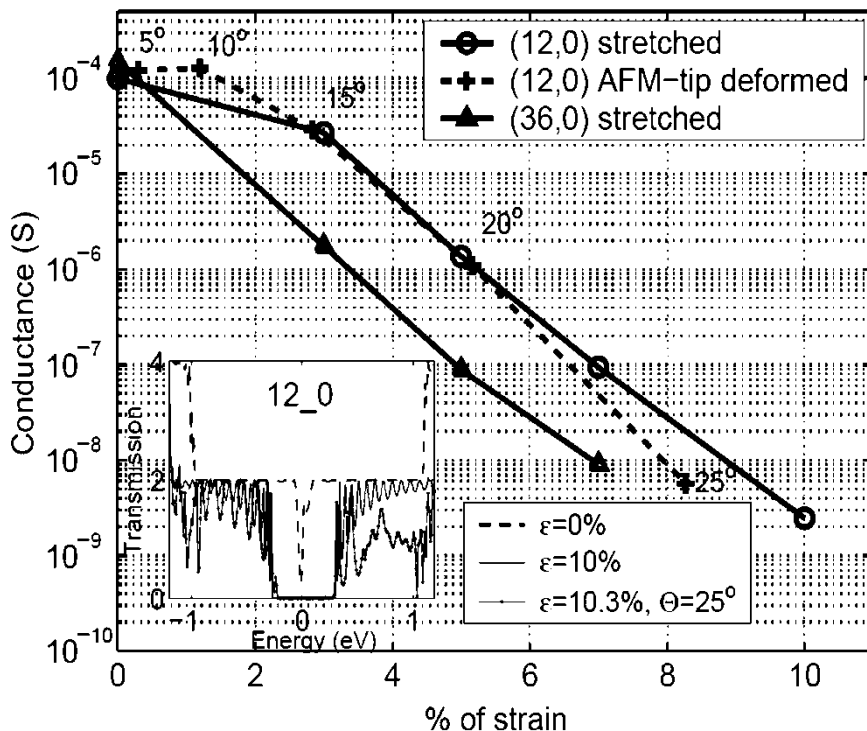
Fig. 2.3 Computed electrical conductance for (12, 0) CNT – comparison between AFM-deformed and uniformly stretched tubes. *Inset* displays density of states plot for the (12, 0) tube at the largest deformations, showing opening of a bandgap at the Fermi energy. The figure also displays the conductance of a (36, 0) tube subjected to a uniform stretch

stretch [56]. Commercial applications from such work could lead to novel pressure sensors, transducers, amplifiers, and logic devices [57].

Finally, progress is also being made in the application of CNTs as actuators [58, 59], where an externally applied small electric voltage, heat, or optical signal is transduced in the form of mechanical deformation of oscillations. Significant insight for the working of such devices can be provided through a theoretical understanding of the mode of electromechanical coupling in a CNT. A few such attempts using both DFT and tight-binding have appeared in the theoretical literature [60].

2.1.2   CNT–Metal Contacts

Conductance through a nanodevice depends strongly on the contact resistance of the metal electrodes, and CNT-based electronic devices are no exception. Besides,

CNTs interacting with metal nanoparticles are gaining considerable interest as sensing materials, catalysts, in the synthesis of metallic nanowires, as well as in nanoelectronics applications as field-effect-transistor (FET) devices. A systematic study of electron-beam-evaporation-coating of suspended CNT with various metals reveals that the nature of the coating can vary significantly depending upon the metal [61]. Thus, Ti, Ni, and Pd form continuous and quasicontinuous coating, while Au, Al, and Fe form only discrete particles on the CNT surface. In fact, Pd is a unique metal in that it consistently yields ohmic contacts to metallic nanotubes [62] and zero or even negative Schottky barrier at junctions [63] with semiconducting CNTs for FET applications. The Schottky barrier (for p-channel conductance) could, in principle, be made even lower if a higher work function metal, e.g., Pt is used. Unfortunately, Pt appears to form nonohmic contacts to both metallic and semiconducting CNTs with lower p-channel conductance than Pd-contacted junctions.

The computed interaction energy of a single metal atom on a CNT [64] follows the trend $E_b(\text{Ti}) >> E_b(\text{Pt}) > E_b(\text{Pd}) > E_b(\text{Au})$. These trends would suggest that Ti sticks the best to the CNT and Au the worst, in good agreement with experiment. However, it does not explain why Pt consistently makes worse contacts than Pd, and why Ti, in spite of its good wetting of a CNT surface, yields Ohmic contacts only rarely [62]. A detailed investigation of the metal–CNT contact at full atomistic detail is a significant undertaking, and is likely beyond the realm of today's first-principles quantum mechanics codes. Nevertheless, as a first attempt, it is instructive to look into the interactions of CNTs with metallic entities beyond single atoms.

We carried out binding energy calculations of metallic monolayers, multilayers, and 13-atom clusters with a sheet of graphene, which is a representative of wide-diameter CNTs. In addition, the interaction of a semiconducting (8, 0) tube with flat metallic surfaces was also studied. Three metals were considered for concreteness – Au, Pt, and Pd. Calculations were performed with the DFT code DMol^3 [3, 29] Details are given in Ref. [65]. We only summarize the main results below:

1. For isolated Au, Pd, and Pt atoms on a sheet of graphene, the respective binding energies are 0.30, 0.94, and 1.65 eV, respectively, i.e., in the same order as previous computed values on a (8, 0) CNT [64]. The binding sites are also quite similar, although the binding energies to graphene are ∼40% smaller than that to the CNT, whose finite curvature imparts higher reactivity.
2. For monolayer or multilayer of metal atoms on graphene, most of the metal binding arises from metal–metal interaction rather than metal–graphene interaction. This is due to high cohesive energies of the metals in the bulk crystalline state. If only the metal–graphene part of the interaction is considered, the binding for Pt falls rapidly with layer thickness, and is less than that of Pd for three-layer films, perhaps indicating possible instability of Pt films beyond a certain thickness. This is likely due to much higher cohesive energy of Pt as compared to that of Pd. For Au, isolated atoms as well as films interact very weakly with graphene, in agreement with experimentally observed poor wetting properties.

3. A 13-atom Pd cluster binds more strongly to the graphene surface than a 13-atom Pt cluster. The Pd cluster, in particular, gets significantly distorted from its ideal icosahedral geometry (see Fig. 2.4). Spin might play an important role in such binding calculations, and requires a more careful analysis.

4. We predict a critical cluster size of a few tens of metal atoms below which the metal should wet a graphene (and therefore CNT) surface uniformly, and above which nonuniform clustering is likely. Using a simple model we show that the critical cluster size for Pt is ~23, which is smaller than that for Pd (~30), implying higher propensity of Pt to form a nonuniform coating unless it is deposited in the form of ultrafine nanoparticles.

5. Finally, CNTs placed on flat Pt or Pd surface can form direct covalent bonds to the metal, which, along with the resulting deformation in tube cross-section might alter its electronic properties and impact performance of electronic devices based on such geometry. Interaction with an Au surface is weak, and the CNT cross-section remains circular.

Our emphasis has been on the structure and chemistry of metal–CNT contacts. In order to characterize the contact resistance one needs to investigate electronic transport across the contact. We would like to mention a few contributions that shed important light into various aspects of this problem: effect of contact geometry and oxide thickness on Schottky barrier [66], effect of tube diameter and gate dielectric constant on current–voltage (I–V) characteristics [67], dependence of
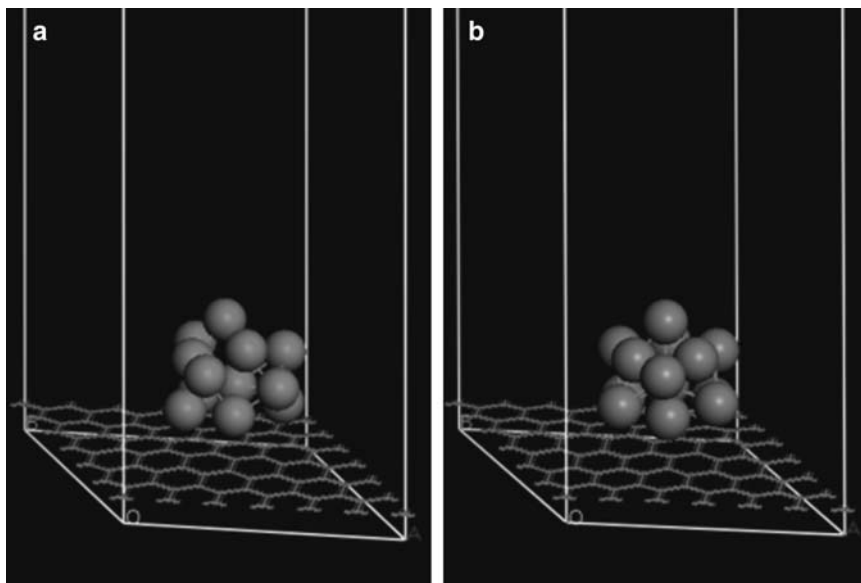
Fig. 2.4 Relaxed structures of (**a**) a 13-atom Pd cluster; and (**b**) a 13-atom Pt cluster on a (6 × 6) graphene surface. The binding energies (for the whole cluster) are 1.2 eV and 0.7 eV, respectively. Smaller Pd–Pd bond strength leads to a more open structure of the Pd-13 cluster and a higher binding energy to the graphene surface

Schottky barrier for various metals and surfaces [68], dependence of contact quality on charge distribution across the contact [69], and controlled lowering of Schottky barrier with chemical treatment [70]. For other theoretical aspects, including a discussion on electron–phonon scattering and effect of disorder on transport, we refer the reader to a recent review by Charlier et al. [71].

2.1.3 SWNTs as Chemical Sensors

Of the projected electronics-based application areas of CNTs, chemical/gas sensors appear to show a lot of commercial promise. Detection of gas molecules such as Ar, NO_2, O_2, NH_3, N_2, CO_2, H_2, CH_4, CO, or even water is important for monitoring environmental, medical, or industrial conditions. It has been reported [72–75] that the measured electrical conductance of semiconducting SWNTs at room temperature can increase or decrease upon the adsorption of different gas molecules. In particular, it was found that [72] the electrical conductance of a p-doped SWNT increases by three orders of magnitude upon exposure to 0.2% of NO_2, and decreases by two orders of magnitude upon exposure to 1% of NH_3. Amine containing molecules have been observed to significantly alter the doping type and the I–V characteristics of CNT-based transistors [76]. Exposure to O_2 also appears to consistently increase the electrical conductance, although the effect is not as dramatic as for NO_2. In addition to the above mentioned changes in electrical conductance, physisorption of molecules on CNTs has led to measurable modulations in capacitance [77] and thermopower [78]. Also, the selectivity and sensitivity of detection can be increased significantly by using appropriate functionalization, e.g., nanotubes coated by polymer [79] and single-stranded DNA [80]. Researchers have also extended nanotube-based sensors to the detection and immobilization of biomolecules and other biorelated applications [81–85].

Measured I–V characteristics of the CNT used in the experiment of Kong et al. [72] identified it to be effectively p-type (i.e. holes were the majority carriers). Thus, the observed behavior of conductance changes can be rationalized through a simple charge transfer model in which NO_2 molecules accept electrons from the CNT, thereby increasing the hole population, while the NH_3 molecules donate electrons, thereby depleting the hole population and the conductance. For NO_2 the computed binding energy has varied between 0.4 and 0.9 kcal mol^{-1} [81], and could be enhanced even more through the formation of NO_3 groups [86–88]. However, such a conclusion for NH_3 is inconsistent with theoretical results [89, 90] showing that NH_3 molecules interact very weakly with pure CNTs, which would make charge transfer very difficult to explain.

A possible explanation could be the presence of topological defects on the CNT incorporated either thermally or during high-temperature growth conditions. Evidence of the importance of defects has appeared in the experimental literature [91, 92]. Also, the nanotubes are not in isolation, and surrounding environment (oxygen, water vapor), or the substrate, or metal contacts at the ends might directly
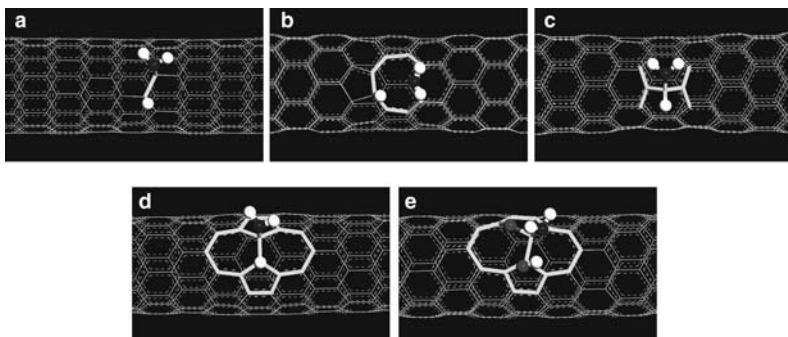
Fig. 2.5 NH$_3$ dissociated at various defects on a (8, 0) CNT: (**a**) defect-free tube; (**b**) vacancy; (**c**) interstitial; (**d**) a Stone–Wales (SW) defect; and (**e**) an O$_2$ molecule predissociated at a SW defect (SW_O_O). Dissociated NH$_2$ and H fragments are shown in *ball* representation. In (**e**), the second O breaks an O–C bond and creates a OH group single-bonded to the other C atom

Table 2.1 NH$_3$ dissociation (into NH$_2$ and H) on a (8, 0) CNT: reaction energetics (ΔE_{reac}), activation barrier (ΔE_{act}), and net electron transfer (Δq) from NH$_2$ and H groups to the CNT

Substrate	Resulting bonding configuration on CNT surface	ΔE_{reac} (eV)	ΔE_{act} (eV)	Δq from NH$_3$ (el)
CNT (defect-free)	C$_3$–NH$_2$ + C$_3$–H (Fig. 2.5a)	+0.77	2.38	0.025
V	C$_2$–NH$_2$ + C$_2$–H (Fig. 2.5b)	−2.49	0.35	0.063
I	NH$_2$–C$_{2,\text{ bridge}}$–H (Fig. 2.5c)	−2.26	1.13	0.036
SW	C$_{3,\,577}$–NH$_2$ + C$_{3,\,577}$–H (Fig. 2.5d)	−0.17	1.50	0.044
SW_O_O	C$_{3,\,577,\,O}$–NH$_2$ + C$_{3,577}$–O–H (Fig. 2.5e)	−2.77	0.25	0.176

Negative values of (ΔE_{reac}) denote an exothermic process
C$_3$ = Regular threefold coordinated sp^2 carbon on a defect-free CNT; C$_2$ = C$_3$ atom with a missing C neighbor; C$_{3,\,577}$ = sp^2 carbon at a SW site shared by two heptagons and a pentagon; C$_{3,\,577,\,O}$ = C$_{3,\,577}$ atom with a bridging O separating it from one of its C neighbors

or indirectly provide a mechanism of binding of the gas molecules [66, 93]. Recently we performed DMol^3 [3] calculations on the chemisorption of a NH$_3$ molecule on structural defects on a semiconducting SWNT [94]. Figure 2.5 displays dissociated NH$_2$ and H fragments chemisorbed on a (8, 0) CNT containing various types of defects: (a) pristine CNT; (b) a vacancy (V); (c) an interstitial (I); (d) a Stone-Wales (SW) defect [95]; and (e) an O$_2$ molecule pre-dissociated into a SW defect (SW_O_O). Table 2.1 displays the reaction energetics (ΔE_{reac}), activation barrier (ΔE_{act}), and net electron transfer (Δq) from NH$_2$ and H groups to the CNT for the five structures described by Fig. 2.5a-e. We follow the convention that $\Delta E_{reac} < 0$ for an exothermic process. The important results can be summarized as follows:

1. Chemisorption to a defect-free CNT is an endothermic process with a large activation barrier, and therefore highly unlikely even at elevated temperatures.

2. At both V and I the dissociation becomes exothermic with energy gains of 2.49 and 2.26 eV, respectively. The activation barrier for dissociation is rather low at V, and dissociation should happen readily at room temperature, while that at I is also possible, although at a slower rate.

3. At SW the dissociation is marginally exothermic, and the activation barrier is lower than that for a defect-free tube, although a bit high for chemisorption to happen readily at room temperatures. However, the presence of pre-dissociated O (SW_O_O) significantly enhances the stability of chemisorbed NH_3 and makes the NH_3 dissociation process nearly spontaneous.

4. In all cases there is net electron transfer from the chemisorbed NH_3 to the CNT. As compared to the defect-free tube, the amount of charge transfer to V increases almost two-and-a-half fold, while that to SW_O_O is enhanced nearly seven-fold. It is also to be noted here that multiple O_2 molecules could potentially dissociate on the same SW defect, thus providing dissociation sites for multiple NH_3 molecules, leading to much higher net charge transfer to the SWNT.

5. Computed infrared (IR) spectrum of some of the defect structures of Fig. 2.5 provides proper interpretation of experimental FTIR data [96]. See Andzelm et al. [94] for more details.

Large charge transfer should qualitatively explain the observed drops in electrical conductance, although a quantitative comparison would require explicit electronic transport calculations [97]. An important part of that problem is an analysis of the electronic density of states (DOS), which has been carried out for several different adsorbates on nanotubes, both physisorbed and chemisorbed [94, 98, 99]. Most important to transport are the changes in DOS that occur close to the Fermi surface. In addition, most of the theoretical analyses have been performed on molecules adsorbing on the external surface of single isolated nanotubes. In reality, the sensor design often involves nanotube networks, bundles, and films. For such systems, one needs to analyze the effect of binding and diffusion in the intertube space within bundles, which could lead to more delayed desorption [100] than for the isolated tubes.

2.2 Metal-Oxide Nanowires

In spite of tremendous advances in carbon nanotube research, there remain some practical difficulties that hinder many applications. Cheap mass-production remains one of the biggest hurdles. Other technological challenges involve controlling CNT diameter, chirality, and doping levels, isolating/separating CNTs from bundles, alignment in nanocomposites, and so on. Chemical inertness of the CNT often poses big problems in sensor applications and adhesion to structural materials, although some of it is being overcome through chemical functionalization. The above deficiencies prompted researchers to explore other types of one-dimensional nanostructures, and led to the synthesis of *nanowires* and *nanoribbons*. Nanowires
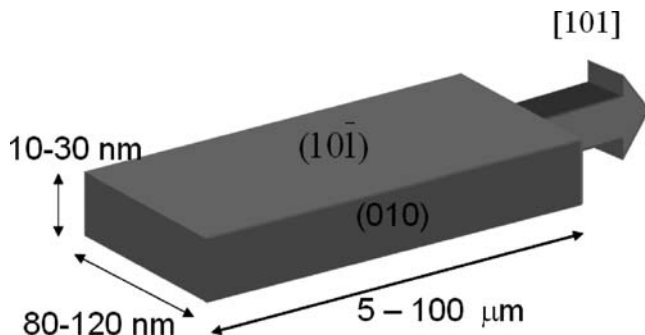
Fig. 2.6 Schematic diagram of a SnO$_2$ nanoribbon, showing typical dimensions, exposed planes, and growth direction

are typically solid (i.e., not hollow) cylindrical objects with a nearly uniform diameter of a few tens of nanometers or less. Most nanowires [101] have so far been synthesized from standard semiconductors: Si, Ge, GaAs, GaP, GaN, InAs, InP, ZnS, ZnSe, CdS, CdSe, and mixed compounds. Semiconducting nanowires have great potential in electronic and optoelectronic applications at the nanoscale. In addition, conducting nanowires made of transition and noble metals, silicides (ErSi$_2$), and polymeric materials have also been investigated in connection with interconnect applications.

Nanoribbons are a special type of nanowires. As the name suggests, they possess a uniform rectangular cross-section with well-defined crystal structure, exposed planes, and growth direction (see Fig. 2.6). So far, nanoribbons have primarily been synthesized from the oxides of metals and semiconductors. In particular, SnO$_2$ and ZnO nanoribbons [102–104] have been material systems of great current interest because of potential applications as catalysts, in optoelectronic devices, and as chemical sensors for pollutant gas species and biomolecules [105–107]. Although they grow to tens of microns long, the nanoribbons are remarkably single-crystalline and essentially free of dislocations. Thus they provide an ideal model for the systematic study of electrical, thermal, optical, and transport processes in one-dimensional semiconducting nanostructures, and their response to various external process conditions.

2.2.1 SnO$_2$ Nanoribbons as Gas Sensor

SnO$_2$ nanoribbons are usually synthesized by evaporating SnO or SnO$_2$ powder at high temperature, followed by deposition on an alumina substrate in the downstream of an Ar-gas flow [102]. Field-emission scanning electron microscopy (FE-SEM) and transmission electron microscopy revealed that the ribbons (1) possess a highly crystalline rutile structure; (2) grow tens of microns long in the <1 0 1> direction; (3) display a uniform quasirectangular cross-section

perpendicular to the growth direction; and (4) present the (1 0 $\bar{1}$) and (0 1 0) rutile planes as surface facets along the growth axis, with dimensions ranging from 80 to 120 nm by 10 to 30 nm (Fig. 2.6). Rutile SnO_2 is a wide-bandgap (3.6 eV) n-doped semiconductor, with the intrinsic carrier density determined by the deviation from stoichiometry, primarily in the form of oxygen vacancies [108]. Experiments with SnO_2 nanoribbons [109] indicate that these are highly effective in detecting even very small amounts of harmful gases like NO_2. Upon adsorption of these gases, the electrical conductance of the sample decreases by several orders of magnitude. More interestingly, it is possible to get rid of the adsorbates by shining UV light, and the electrical conductance is completely restored to its original value. Such single-crystalline sensing elements have several advantages over conventional thin-film oxide sensors: low operating temperatures, no ill-defined coarse grain boundaries, and high active surface-to-volume ratio.

Electron withdrawing groups like NO_2 and O_2 are expected to deplete the conduction electron population in the nanoribbon, thereby leading to a decrease in electrical conductance. To investigate this, we performed $DMol^3$ calculations of the adsorption process of NO_2, O_2 and CO on the exposed (1 0 $\bar{1}$) and (0 1 0) surfaces, as well as the edge atoms of a SnO_2 nanoribbon [110]. The nanoribbon surfaces were represented in periodic supercells (Fig. 2.7).

In bulk rutile SnO_2, the Sn atoms are octahedrally coordinated with six O neighbors, while each O atom is a threefold bridge between neighboring Sn centers. At both (1 0 $\bar{1}$) and (0 1 0) surfaces the Sn atoms lose an O neighbor, thereby becoming fivefold coordinated (Fig. 2.7a, b). The surface O atoms become twofold-coordinated bridges connecting neighboring surface Sn atoms (Fig. 2.7a, b). Both surfaces were represented by three layers of Sn, each layer being sandwiched between two O layers. The bottom SnO_2 layer was fixed in order to simulate the presence of several bulk-like layers in the actual sample. In order to reduce interaction with periodic images, the surface unit cell was doubled in the direction
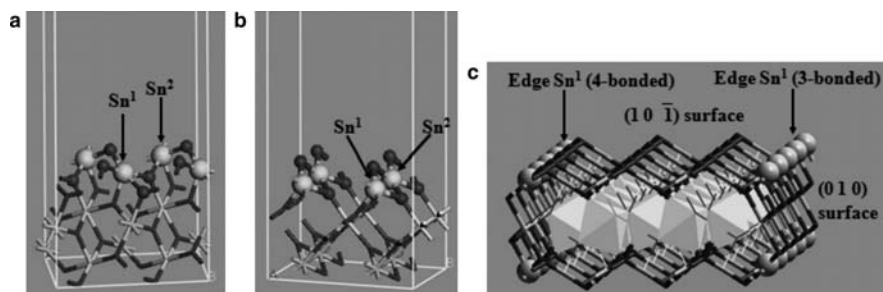
Fig. 2.7 Simulation supercells representing exposed surfaces of a SnO_2 nanoribbon: (**a**) (1 0 $\bar{1}$) surface; (**b**) (0 1 0) surface; and (**c**) nanoribbon edge. For clarity, the periodic cell is not shown in (**c**), and the interior atoms are represented by *polyhedra*. Surface atoms in (**a**) and (**b**), and edge atoms in (**c**) are shown in *ball* representation. *Larger balls* and *smaller balls* represent Sn and O atoms, respectively. Sn^1 and Sn^2 are neighboring Sn atoms connected with a bridging O. Reprinted with permission from Ref. [110]. Copyright (2005) from the American Chemical Society

of the smaller surface lattice constant, and a vacuum of 15 Å was placed normal to the surface. To simulate nanoribbon edges [i.e., lines of intersection of $(1\ 0\ \bar{1})$ and $(0\ 1\ 0)$ planes], a structure as in Fig. 2.7c was embedded in a periodic supercell with the smallest repeat period (5.71 Å) along the length of the ribbon, and a vacuum of 15 Å normal to both the $(1\ 0\ \bar{1})$ surface (y-axis) and the $(0\ 1\ 0)$ surface (x-axis). At the nanoribbon edges the Sn atoms can be either threefold- or fourfold-coordinated (Fig. 2.7c).

Details of the results on binding energy and charge transfer are discussed elsewhere [110]. The important results are summarized below.

All adsorbate structures involve one or more bonds to surface Sn atoms. The binding energy on different surfaces and edges increases in the sequence $(0\ 1\ 0) <$ $(1\ 0\ \bar{1}) <$ threefold edge $<$ fourfold edge.

NO_2 adsorption displays a very rich chemistry because it can either form a single bond to a surface Sn, or can adsorb in the bidented form through two single bonds to neighboring Sn atoms. The doubly bonded NO_2 is 2–3 kcal mol^{-1} more stable than the single-bonded NO_2, and the binding energies are in general 4–5 kcal mol^{-1} higher on the $(1\ 0\ \bar{1})$ surface than on the $(0\ 1\ 0)$. Activation barrier between the doubly-bonded and single-bonded structures is expected to be low, which should make the NO_2 species mobile on the exposed faces by performing a series of random walk steps along well-defined rows of Sn atoms on the surface.

When two NO_2 molecules meet on the surface, either through random walk as described above, or through the incidence of a second NO_2 from gas phase in the vicinity of an already chemisorbed NO_2, there is a transfer of an O atom from one NO_2 to the other, thus converting it to a surface NO_3 species. The net disproportionation reaction $NO_2 + NO_2 \rightarrow NO_3 + NO$ is well known in chemistry. The bidented NO_3 group has a substantially higher binding energy, especially on the $(1\ 0\ \bar{1})$ surface, and should not therefore be mobile. The resulting NO species is only weakly bound to the surface and should desorb easily. Synchrotron measurements using X-ray absorption near-edge spectroscopy (XANES) confirmed the abundance of NO_3 species on the nanoribbon surface following NO_2 adsorption.

On a defect-free surface (i.e., surface with no O-vacancies), the O_2 molecules can only weakly physisorb. In this configuration, there is no charge transfer to the O_2, and therefore, a nanoribbon surface without surface O-vacancies should be insensitive to atmospheric oxygen. However, at O-vacancy sites, the O_2 molecule has a strongly bound chemisorbed structure in the form of a peroxide bridge.

Both NO_3 groups and chemisorbed O_2 (at O-vacancy sites) accept significant amount of electronic charge from the surface. Therefore, such adsorbates should lead to the lowering of electrical conductance of the effectively n-doped sample. CO, on the other hand, donates a moderate amount of electrons to the surface, and is therefore expected to increase the electrical conductance. All these results are consistent with direct experimental measurements of sample conductance [105, 109, 111]. Charge transfer between molecular species (donor or acceptor alike) and the nanoribbon surface could thus serve as a general mechanism for ultrasensitive chemical and biological sensing using single crystalline semiconductor nanowires.

A CO likes to adsorb in the following manner: the C forms two single bonds to the surface – one with a surface Sn and another with a bridging O, while the O of the CO forms a double bond to the C and sticks out of the surface. This way, the C atoms attains its preferred 4-valency and the O has its bivalency satisfied.

To end this section, we would like to note that pioneering work by Lieber and his network of collaborators has led to the synthesis and exploration of many different configurations of nanowires, including core-shell structures, cross-bar architecture, heterostructures, and so on. Versatility in materials choice and architectural flexibility are enabling a vast array of potential applications including optical waveguides, nanophotonics, nanomedicine, NEMS, biosensing, biomedicine, flexible electronics, and smart materials. For a recent review see Ref. [112]. Some of the previous work has been reviewed by Law et al. [113].

2.3   Conclusions

Through a few application examples we have illustrated the use of a variety of theoretical techniques spanning a wide spectrum of length and time-scales. As better synthesis and experimental manipulation methods emerge, and more complex and newer applications are proposed, they open up exciting opportunities for theory, modeling, and simulations. However, several challenges, both experimental and theoretical, remain as a roadblock to successful commercial deployment of most technologies. As with any nanosystem, contact remains a critical issue. Small atomic-level changes in the structure of the contact can have a significant impact on the contact resistance, and very little characterization data exists on most experimental contacts. Besides, even though DFT-based NEGF codes are becoming faster and more accurate, they are still too limited in realistically representing metal–CNT contacts. Standard DFT or tight-binding treatments, as described here, also do not take into account complex many-body electron-correlation effects that may arise at low temperatures, or Coulomb blockade effects when electrons in CNTs get highly localized because of large mechanical deformation or highly resistive contacts.

References

1. Mintmire, J. W.; Dunlap, B. I.; White, C. T., Are fullerene tubules metallic, *Phys. Rev. Lett.* **1992**, 68, 631–634

2. Hamada, N.; Sawada, S.; Oshiyama, A., New one-dimensional conductors: Graphitic micro-tubules, *Phys. Rev. Lett.* **1992**, 68, 1579–1582

3. Saito, R.; Fujita, M.; Dresselhaus, G.; Dresselhaus, M. S., Electronic structure of chiral graphene tubules, *Appl. Phys. Lett.* **1992**, 60, 2204–2206

4. White, C. T.; Robertson, D. H.; Mintmire, J. W., Helical and rotational symmetries of nanoscale graphitic tubules, *Phys. Rev. B* **1993**, 47, 5485–5488

5. Jishi, R. A.; Inomata, D.; Nakao, K.; Dresselhaus, M. S.; Dresselhaus, G., Electronic and lattice properties of carbon nanotubes, *J. Phys. Soc. Jpn* **1994**, 63, 2252–2260

6. White, C. T.; Mintmire, J. W.; Mowrey, R. C.; Brenner, D. W.; Robertson, D. H.; Harrison, J. A.; Dunlap, B. I., In Buckminsterfullerenes; Billups, W. E.; Ciufolini, M. A., Eds.; VCH Publishers, Deerfield Beach, FL, 1993

7. Articles in *Phys. World* **2000**, 13, 29–53

8. Terrones, M., Science and technology of the twenty-first century: Synthesis, properties, and applications of carbon nanotubes, *Annu. Rev. Mater. Res.* **2003**, 33, 419–501

9. Baughman, R. H.; Zakhidov, A. A.; de Heer, W. A., Carbon nanotubes - The route toward applications, *Science* **2002**, 297, 787–792

10. Ajayan, P. M.; Zhou, O., in Carbon Nanotubes Synthesis, Structure, Properties and Applications; Dresselhaus, M. S.; Dresselhaus, G.; Avouris, P., Eds.; Springer, Berlin, **2001**, 391–425

11. Meyyappan, M., Ed., Carbon Nanotubes – Science and Applications, CRC, Boca Raton, FL, **2004**

12. Iijima, S., Helical microtubules of graphitic carbon, *Nature* **1991**, 354, 56–58

13. Articles in NSTI Technical Proceedings, NSTI Publications, Cambridge, MA, Vol. 2, **2001**

14. Articles in NSTI Technical Proceedings, NSTI Publications, Cambridge, MA, Vol. 2, **2002**

15. Articles in NSTI Technical Proceedings, NSTI Publications, Cambridge, MA, Vol. 3, **2003**

16. Bernholc, J.; Brenner, D.; Nardelli, M. B.; Meunier, V.; Roland, C., Mechanical and electrical properties of nanotubes, *Annu. Rev. Mater. Res.* **2002**, 32, 347–375

17. Tománek, D.; Enbody, R., Eds., Science and Applications of Nanotubes, Kluwer, Netherlands, **2000**

18. Articles in *Phys. B*: *Condensed Matter* **2002**, 323, No. 1–4

19. Tombler, T. W.; Zhou, C.; Alexseyev, L.; Kong, J.; Dai, H.; Liu, L.; Jayanthi, C. S.; Tang, M.; Wu, S. Y., Reversible electromechanical characteristics of carbon nanotubes under local-probe manipulation, *Nature* **2000**, 405, 769–772

20. Nardelli, M.; Bernholc, J., Mechanical deformations and coherent transport in carbon nanotubes, *Phys. Rev. B* **1999**, 60, R16338–R16341

21. Rochefort, A.; Avouris, P.; Lesage, F.; Salahub, D., Electrical and mechanical properties of distorted carbon nanotubes, *Phys. Rev. B* **1999**, 60, 13824–13830

22. Liu, L.; Jayanthi, C. S; Dai, H., Controllable reversibility of an sp^2 to sp^3 transition of a single wall nanotube under the manipulation of an AFM tip: A nanoscale electromechanical switch, *Phys. Rev. Lett.* **2000**, 84, 4950–4953

23. Parr, R. G.; Yang, W., Density Functional Theory of Atoms and Molecules, Oxford University Press, Oxford, **1989**

24. Hohenberg, P.; Kohn, W., Inhomogeneous electron gas, *Phys. Rev.* **1964**, 136, B864–B871

25. Kohn, W.; Sham, L. J., Self-consistent equations including exchange and correlation effects, *Phys. Rev.* **1965**, 140, A1133–A1138

26. Jensen, F., Introduction to Computational Chemistry, Wiley, New York, **1999**

27. Hill, J.-R.; Subramanian, L.; Maiti, A., Molecular Modeling Techniques in Material Sciences, CRC/Taylor & Francis, Boca Raton, FL/London, **2005**

28. Rappe, A. K.; Casewit, C. J.; Colwell, K. S.; Goddard, W. A.; Skiff, W. M., UFF: A full periodic table force field for molecular mechanics and molecular dynamics simulations, *J. Am. Chem. Soc.* **1992**, 114, 10024–10039

29. Delley, B., An all-electron numerical method for solving the local density functional for polyatomic molecules, *J. Chem. Phys.* **1990**, 92, 508–517

30. Delley, B., Fast calculation of electrostatics in crystals and large molecules, *J. Phys. Chem.* **1996**, 100, 6107–6110

31. Delley, B., A scattering theoretic approach to scalar relativistic corrections on bonding, *Int. J. Quantum Chem.* **1998**, 69, 423–433

32. Delley B., From molecules to solids with the DMol[3] approach, *J. Chem. Phys.* **2000**, 113, 7756–7764

33. Perdew, J. P.; Burke, K.; Ernzerhof, M., Generalized gradient approximation made simple, *Phys. Rev. Lett.* **1996**, 77, 3865–3868

34. Monkhorst, H. J.; Pack, J. D., Special points for Brillouin-zone integrations, *Phys. Rev. B* **1976**, 13, 5188–5192

35. Szabo, A.; Ostlund, N. S., Modern Quantum Chemistry, Dover, New York, **1996**

36. Maiti, A., Application of carbon nanotubes as electromechanical sensors – Results from First-Principles simulations, *Phys. Stat. Sol. B* **2001**, 226, 87–93

37. Datta, S., Electronic Transport in Mesoscopic Systems, Cambridge University Press, Cambridge, **1997**

38. Datta, S., Quantum Transport: Atom to Transistor, Cambridge University Press, Cambridge, **2005**

39. Imry, Y., Introduction to Mesoscopic Physics, Oxford University Press, Oxford, **1997**

40. Brandbyge, M.; Mozos, J.; Ordejón, P.; Taylor, J.; Stokbro, K., Density-functional method for nonequilibrium electron transport, *Phys. Rev. B* **2002**, 65, 165401.1–165401.17

41. Ferry, D. K.; Goodnick, S. M., Transport in Nanostructures, Cambridge University Press, Cambridge, **1997**

42. Beenakker, C. W. J., Random-matrix theory of quantum transport, *Rev. Mod. Phys.* **1997**, 69, 731–808

43. Büttiker, M., Four-terminal phase-coherent conductance, *Phys. Rev. Lett.* **1986**, 57, 1761–1764

44. Landauer, R., Conductance determined by transmission: Probes and quantised constriction resistance, *J. Phys.: Condens: Matter* **1989**, 1, 8099–8110

45. Papaconstantopoulos, D. A.; Mehl, M. J.; Erwin, S. C.; Pederson, M. R., Tight-binding approach to computational materials science, In MRS Proceedings 491; Turchi, P.E.A.; Gonis, A.; Colombo, L., Eds.; Materials Research Society, Warrendale, PA, **1998**

46. Maiti, A.; Svizhenko, A.; Anantram, M. P., Electronic transport through carbon nanotubes: Effects of structural deformation and tube chirality, *Phys. Rev. Lett.* **2002**, 88, 126805.1–126805.4

47. Kane, C. L.; Mele, E. J., Size, shape, and low energy electronic structure of carbon nanotubes, *Phys. Rev. Lett.* **1997**, 78, 1932–1935

48. Heyd, R.; Charlier, A.; McRae, E., Uniaxial-stress effects on the electronic properties of carbon nanotubes, *Phys. Rev. B* **1997**, 55, 6820–6824

49. Yang, L.; Anantram, M. P.; Han, J.; Lu, J. P., Band-gap change of carbon nanotubes: Effect of small uniaxial and torsional strain, *Phys. Rev. B* **1999**, 60, 13874–13878

50. Yang, L.; Han, J., Electronic structure of deformed carbon nanotubes, *Phys. Rev. Lett.* **2000**, 85, 154–157

51. Kleiner, A.; Eggert, S., Band gaps of primary metallic carbon nanotubes, *Phys. Rev. B* **2001**, 63, 073408.1–073408.4

52. Lammert, P. E.; Zhang, P.; Crespi, V. H., Gapping by squashing: Metal–insulator and insulator-metal transitions in collapsed carbon nanotubes, *Phys. Rev. Lett.* **2000**, 84, 2453–2456

53. Lu, J-Q.; Wu, J.; Duan, W.; Liu, F.; Zhu, B. F.; Gu, B. L., Metal-to-semiconductor transition in squashed armchair carbon nanotubes, *Phys. Rev. Lett.* **2003**, 90, 156601.1–156601.4

54. Svizhenko, A.; Mehrez, H.; Anantram, M. P.; Maiti, A., Sensing mechanical deformation in carbon nanotubes by electrical response: A computational study, *Proc. SPIE* **2005**, 5593, 416–428

55. Minot, E. D.; Yaish, Y.; Sazonova, V.; Park, J-Y.; Brink, M.; McEuen, P. L., Tuning carbon nanotube band gaps with strain, *Phys. Rev. Lett.* **2003**, 90, 156401.1–156401.4

56. Cao, J.; Wang, Q.; Dai, H., Electromechanical properties of metallic, quasimetallic, and semiconducting carbon nanotubes under stretching, *Phys. Rev. Lett.* **2003**, 90, 157601.1–157601.4

57. Maiti, A., Carbon nanotubes: Band gap engineering with strain, *Nat. Mater. (London)* **2003**, 2, 440–442

58. Baughman, R. H., et al., Carbon nanotube actuators, *Science* **1999**, 284, 1340–1344

59. Sazonova, V.; Yaish, Y.; Ustunel, H.; Roundy, D.; Arias, T. A.; McEuen P. L., A tunable carbon nanotube electromechanical oscillator, *Nature* **2004**, 431, 284–287

60. Hartman, A. Z.; Jouzi, M.; Barnett, R. L.; Xu, J. M, Theoretical and experimental studies of carbon nanotube electromechanical coupling, *Phys. Rev. Lett.* **2004**, 92, 236804.1–236804.4

61. Zhang, Y.; Franklin, N. W.; Chen, R. J.; Dai, H., Metal coating on suspended carbon nanotubes and its implication to metal–tube interaction, *Chem. Phys. Lett.* **2000**, 331, 35–41

62. Mann, D.; Javey, A.; Kong, J.; Wang, Q.; Dai, H., Ballistic transport in metallic nanotubes with reliable Pd ohmic contacts, *Nano Lett.* **2003**, 3, 1541–1544

63. Javey, A.; Guo, J.; Wang, Q.; Lundstrom, M.; Dai, H., Ballistic carbon nanotube field-effect transistors, *Nature* **2003**, 424, 654–657

64. Durgun, E.; Dag, S.; Bagci, V. M. K.; Gülseren, O.; Yildirim, T.; Ciraci, S., Systematic study of adsorption of single atoms on a carbon nanotube, *Phys. Rev. B* **2003**, 67, 201401.1–201401.4

65. Maiti, A.; Ricca, A., Metal–nanotube interactions – binding energies and wetting properties, *Chem. Phys. Lett.* **2004**, 395, 7–11

66. Heinze, S.; Tersoff, J.; Martel, R.; Derkcke, V.; Appenzeller, J.; Avouris, P., Carbon nanotubes as Schottky barrier transistors, *Phys. Rev. Lett.* **2002**, 89, 106801.1–106801.4

67. Guo, J.; Datta, S.; Lundstrom, M., A numerical study of scaling issues for Schottky-barrier carbon nanotube transistors, *IEEE Trans. Electron Devices* **2004**, 51, 172–177

68. Shan, B.; Cho, K. J., Ab initio study of Schottky barriers at metal-nanotube contacts, *Phys. Rev. B* **2004**, 70, 233405.1–233405.4

69. Nemec, N.; Tomanek, D.; Cuniberti, G., Contact dependence of carrier injection in carbon nanotubes: An ab initio study, *Phys. Rev. Lett.* **2006**, 96, 076802.1–076802.4

70. Auvray, S. et al., Chemical optimization of self-assembled carbon nanotube transistors, *Nano Lett.* **2005**, 5, 451–455

71. Charlier, J. C.; Blasé, X.; Roche, S., Electronic and transport properties of nanotubes, *Rev. Mod. Phys.* **2007**, 79, 677–732

72. Kong, J.; Franklin, N.R; Zhou, C.; Chapline, M.G.; Peng, S.; Cho, K.; Dai, H., Nanotube molecular wires as chemical sensors, *Science* **2000**, 287, 622–625

73. Collins, P.G.; Bradley, K.; Ishigami, M.; Zettl, A., Extreme oxygen sensitivity of electronic properties of carbon nanotubes, *Science* **2000**, 287, 1801–1804

74. Valentini, L.; Armentano, I.; Kenny, J. M.; Cantalini, C.; Lozzi, L.; Santucci, S., Sensors for sub-ppm NO_2 gas detection based on carbon nanotube thin films, *Appl. Phys. Lett.* **2003**, 82, 961–963

75. Chopra, S.; McGuire, K.; Gothard, N.; Rao, A. M.; Pham, A., Selective gas detection using a carbon nanotube sensor, *Appl. Phys. Lett.* **2003**, 83, 2280–2282

76. Klinke, C.; Chen, J.; Afzali, A.; Avouris, P., Charge transfer induced polarity switching in carbon nanotube transistors, *Nano Lett.* **2005**, 5, 555–558

77. Snow, E. S.; Perkins, F. K.; Houser, E. J.; Badescu, S. C.; Reinecke, T. L., Chemical detection with a single-walled carbon nanotube capacitor, *Science* **2005**, 307, 1942–1945

78. Sumanasekera, G. U.; Pradhan, B. K.; Romero, H. E.; Adu, K. W.; Eklund, P. C., Giant thermopower effects from molecular physisorption on carbon nanotubes, *Phys. Rev. Lett.* **2002**, 89, 166801.1–166801.4

79. Qi, P.; Vermesh, O.; Grecu, M.; Javey, A.; Wang, Q.; Dai, H.; Peng, S.; Cho, K., Toward large arrays of multiplex functionalized carbon nanotube sensors for highly sensitive and selective molecular detection, *Nano Lett.* **2003**, 3, 347–351

80. Staii, C.; Johnson, A. T.; Chen, M.; Gelperin, A., DNA-decorated carbon nanotubes for chemical sensing, *Nano Lett.* **2005**, 5, 1774–1778

81. Dai, H., Carbon nanotubes: Synthesis, integration, and properties, *Acc. Chem. Res.* **2002**, 35, 1035–1044

82. Chen, R.; Zhang, Y.; Wang, D.; Dai, H., Noncovalent sidewall functionalization of single-walled carbon nanotubes for protein immobilization, *J. Am. Chem. Soc.* **2001**, 123, 3838–3839

83. Grüner, G., Carbon nanotube transistors for biosensing applications, *Anal. Bioanal. Chem.* **2006**, 384, 322–335

84. Heath, J. R. In Nanobiotechnology II; Mirkin, C.; Niemeyer, C. M., Eds.; Wiley, New York, 2007, Chap. 12, 213

85. Asuri, P.; Bale, S. S.; Pangule R. C.; Shah, D. A.; Kane, R. S.; Dordick, J. S., Structure, function, and stability of enzymes covalently attached to single-walled carbon nanotubes, *Langmuir* **2007**, 23, 12318–12321

86. Peng, S.; Cho, K. J.; Qi, P.; Dai, H., Ab initio study of CNT NO_2 gas sensor, *Chem. Phys. Lett.* **2004**, 387, 271–276

87. Rodriguez, J. A.; Jirsak, T.; Sambasiban, S.; Fischer, D.; Maiti, A., Chemistry of NO_2 on CeO_2 and MgO: Experimental and theoretical studies on the formation of NO_3, *J. Chem. Phys.* **2000**, 112, 9929–9939

88. Rodriguez, J. A.; Jirsak, T.; Liu, G.; Hrbek, J.; Dvorak, J.; Maiti, A., Chemistry of NO_2 on oxide surfaces: Formation of NO_3 on $TiO_2(110)$ and NO_2:O vacancy interactions, *J. Am. Chem. Soc.* **2001**, 123, 9597–9605

89. Chang, H.; Lee, J. D.; Lee, S. M.; Lee, Y. H., Adsorption of NH_3 and NO_2 molecules on carbon nanotubes, *Appl. Phys. Lett.* **2001**, 79, 3863–3865

90. Zhao, J.; Buldum, A.; Han, J.; Lu, J. P., Gas molecule adsorption in carbon nanotubes and nanotube bundles, *Nanotechnology* **2002**, 13, 195–200

91. Valentini, L.; Mercuri, F.; Armentano, I.; Cantalini, C.; Picozzi, S.; Lozzi, L.; Santucci, S.; Sgamellotti, A.; Kenny, A., Role of defects on the gas sensing properties of carbon nanotubes thin films: Experiment and theory, *Chem. Phys. Lett.* **2004**, 387, 356–361

92. Robinson, J. A.; Snow, E. S.; Bǎdescu, S. C.; Reinecke, T. L.; Perkins, F. K., Role of defects in single-walled carbon nanotube chemical sensors, *Nano Lett.* **2006**, 6, 1747–1751

93. Yamada, T., Modeling of carbon nanotube Schottky barrier modulation under oxidizing conditions, *Phys. Rev. B* **2004**, 69, 125408.1–125408.8

94. Andzelm, J.; Govind, N.; Maiti, A., Carbon nanotubes as gas sensors – Role of structural defects, *Chem. Phys. Lett.* **2006**, 421, 58–62

95. Stone, A. J.; Wales, D. J., Theoretical studies of icosahedral C_{60} and some related species, *Chem. Phys. Lett.* **1986**, 128, 501–503

96. Ellison, M. D.; Crotty, M. J.; Koh, D.; Spray, R. L.; Tate, K. E., Adsorption of NH_3 and NO_2 on single-walled carbon nanotubes, *J. Phys. Chem. B* **2004**, 108, 7938–7943

97. Maiti, A., Multiscale modeling with carbon nanotubes, *Microelectron. J.* **2008**, 39, 208–221

98. Latil, S.; Roche, S.; Charlier, J. C., Electronic transport in carbon nanotubes with random coverage of physisorbed molecules, *Nano Lett.* **2005**, 5, 2216–2219

99. Santucci, S.; Picozzi, S.; Di Gregorio; F., Lozzi; L., Cantalini, C.; L'Aquila, C.; Valentini, L.; Kenny, J. M.; Delley, B., NO_2 and CO gas adsorption on carbon nanotubes: Experiment and theory, *J. Chem. Phys.* **2003**, 119, 10904–10910

100. Ulbricht, H.; Kriebel, J.; Moos, G.; Hertel, T., Desorption kinetics and interaction of Xe with single-wall carbon nanotube bundles, *Chem. Phys. Lett.* **2002**, 363, 252–260

101. Wang, Z. L., Ed., Nanowires and Nanobelts: Materials, Properties, and Devices, Kluwer, Netherlands, **2003**

102. Dai, Z. R.; Pan, Z. W.; Wang, Z. L., Ultra-long single crystalline nanoribbons of tin oxide, *Solid State Commun.* **2001**, 118, 351–354

103. Huang, M.; Wu, Y.; Feick, H.; Tran, N.; Weber, E.; Yang, P., Catalytic growth of zinc oxide nanowires by vapor transport, *Adv. Mater.* **2001**, 13, 113–116

104. Huang, M.; Mao, S.; Feick, H.; Yan, H.; Wu, Y.; Kind, H.; Weber, E.; Russo, R.; Yang, P., Room-temperature ultraviolet nanowire nanolasers, *Science* **2001**, 292, 1897–1899

105. Comini, E.; Faglia, G.; Sberveglieri, G.; Pan, Z.; Wang, Z. L., Stable and highly sensitive gas sensors based on semiconducting oxide nanobelts, *Appl. Phys. Lett.* **2002**, 81, 1869–1871

106. Cui, Y.; Wei, Q.; Park, H.; Lieber, C. M., Nanowire nanosensors for highly sensitive and selective detection of biological and chemical species, *Science* **2001**, 293, 1289–1292

107. Favier, F.; Walter, E. C.; Zach, M. P.; Benter, T.; R. M. Penner, Hydrogen sensors and switches from electrodeposited palladium mesowire arrays, *Science* **2001**, 293, 2227–2231

108. Founstadt, C. G.; Rediker, R. H., Electrical properties of high-quality stannic oxide crystals, *J. Appl. Phys.* **1971**, 42, 2911–2918

109. Law, M.; Kind, H.; Kim, F.; Messer, B.; Yang, P., Photochemical sensing of NO_2 with SnO_2 nanoribbon nanosensors at room temperature, *Angew. Chem. Int. Ed.* **2002**, 41, 2405–2408

110. Maiti, A.; Rodriguez, J.; Law, M.; Kung, P.; McKinney, J.; Yang, P., SnO_2 nanoribbons as NO_2 sensors: insights from First-Principles calculations, *Nano Lett.* **2003**, 3, 1025–1028

111. Kind, H.; Yan, H.; Law, M.; Messer, B.; Yang, P., Nanowire ultraviolet photodetectors and optical switches, *Adv. Mater.* **2002**, 14, 158–160

112. Lieber, C. M.; Wang, Z. L., Functional nanowires, *MRS Bull.* **2007**, 32, 99–104

113. Law, M.; Goldberger, J.; Yang, P., Semiconductor nanowires and nanotubes, *Annu. Rev. Mater. Res.* **2004**, 34, 83–122